Rare Met.
https://doi.org/10.1007/s12598-024-02891-7

RARE METALS

ORIGINAL ARTICLE

Ni_3S_2@MoS_2 nano-arrays with Mo atomic site as efficient photoanode materials for photoelectrocatalytic inactivation of antibiotic-resistance bacteria and degradation of antibiotic-resistance gene

Jing-Ting Yang, Tao Xu, Pan-Di Lv, Yue Su, Jing Xie, Zhen-Xing Li*, Huan Zhou, Peng-Peng Chen

Received: 8 February 2024 / Revised: 21 March 2024 / Accepted: 25 March 2024

Abstract In this paper, hierarchical ultra-thin core/shell Ni_3S_2@MoS_2 nano-arrays with Mo atomic site grown on nickel foam (Ni_3S_2@MoS_2-NF) were designed and synthesized through the hydrothermal method. When they are tested as photoelectric catalysis electrodes to anti-bacteria, the Ni_3S_2@MoS_2 within core/shell structure exhibits about several times higher rate capability and outstanding cycling stability than traditional photocatalysts. After reacting with water and oxygen, large numbers of extracellular reactive oxygen species on the surface of Ni_3S_2@MoS_2 are observed. These reactive oxygen species can penetrate bacterial cells, resulting in a rapid rise of intracellular reactive oxygen species in a short time. The integrity of the bacterial cell membrane is also destroyed, which can be observed in both scanning and transmission images. The synthetic primer was used to specifically label the gene fragment with antibiotic resistance, which was oxidized and eliminated after the photoelectron catalysis (PEC) reaction, proving that this material for PEC antibacterial can not only kill bacteria. Successful elimination of antibiotic-resistance gene fragments can also be achieved.

Keywords Photoelectric catalysis; Antibiotic-resistance bacteria; Visible light; Antibiotic-resistance gene; Reactive oxygen species; Mo atomic site

1 Introduction

With the excessive use of antibiotics in clinical medicine, many antibiotic-resistant bacteria (ARB) have been found in various external environments. Some bacteria are specifically resistant to different kinds of antibiotics [1]. Antibiotic-resistance genes (ARGs) from dead bacteria can even move to surplus living bacteria in the environment by means of microbial-level gene transfer [2, 3]. To overcome the current shortage of water resources, wastewater recycling is regarded as one of the most effective approaches. Nevertheless, the existence of ARB and ARGs highlights the difficulty in the purification of wastewater [4–6].

To minimize the utilization of antibiotics, it is urgent to exploit eco-friendly and efficient antibacterial materials [7]. Metal-ions-assistant treatment, ultraviolet (UV) irradiation and advanced chemical oxidant processes are the most common methods used over the past decades; however, each of these approaches suffers from somewhat limitations [8, 9]. The utilization of heavy metals (e.g., Ag

Jing-Ting Yang and Tao Xu have contributed equally to this work.

Supplementary Information The online version contains supplementary material available at https://doi.org/10.1007/s12598-024-02891-7.

J.-T. Yang, P.-D. Lv, P.-P. Chen
Anhui Province Key Laboratory of Environment-Friendly Polymer Materials, School of Chemistry and Chemical Engineering, Anhui University, Hefei 230601, China

T. Xu
Inflammation and Immune Mediated Diseases Laboratory of Anhui Province, Anhui Institute of Innovative Drugs, School of Pharmacy, Anhui Medical University, Hefei 230032, China

Y. Su, J. Xie, H. Zhou
National Institute of Clinical Drug Trials, The First Affiliated Hospital of Bengbu Medical University, Bengbu 233030, China

Z.-X. Li*
State Key Laboratory of Heavy Oil Processing, College of New Energy and Materials, China University of Petroleum (Beijing), Beijing 102249, China
e-mail: lizx@cup.edu.cn

Published online: 03 August 2024

and Cu) negatively affects human bodies and provokes secondary environmental pollution. Physical irradiation as an original sterilization method can only use ultraviolet wavelength, resulting in a low utilization rate of a light wave. For example, Ferro et al. [10] found that the antibiotic-resistant bacteria were utterly inactivated after UV/H_2O_2 treatment over 300 min, while the target ARG still existed in the water suspension. Previous results directly demonstrate that UV irradiation exhibits rather limited efficiency in degrading ARG in water [11]. The advanced chemical oxidation process such as adsorption, photocatalysis and Fenton homogeneous photocatalysis can be regarded as another effective solution [12–14]. However, Fenton oxidation is generally carried out under the limitation of pH 2–5, and its efficiency is significantly depressed by the reduced utilization rate of hydroxyl radical due to the side reaction between Fe^{2+} and hydrogen peroxide.

The generation of reactive oxygen species (ROS) by a photocatalytic process is an efficient and eco-friendly method to trigger sterilization. Bacteria are attacked by ROS and subsequently break down into cell membranes, DNA and mitochondria, thus causing their death [15, 16]. ROS (e.g., $^1O_2$, ·OH, $\cdot O_2^-$) can be produced over photocatalyst in the photocatalytic sterilization process, exhibiting powerful oxidation capacity to damage the cell membrane, lipids, proteins and genetic material of bacteria [17, 18]. Photocatalysts, such as TiO_2 and MoS_2, have the advantages of good sterilization efficiency, high stability, low cost, easy preparation, green non-toxic, etc., thus frequently used as candidates to inactivate bacteria [19]. However, the application of these photocatalytic techniques is also limited. First of all, most of the photocatalysts prepared in powder form are challenging to recapture from water, thus resulting in secondary pollution to the aquatic environment. Secondly, the severe recombination of electron–hole pairs generally reduces the catalytic activity of photocatalysts [20].

Sunlight is the most abundant and inexhaustible energy source on Earth. However, its low energy density, dispersibility and intermittent nature make its direct utilization with industrial relevance challenging, suggesting that converting sunlight into chemical energy and storing it is a valuable measure. The photoelectron catalysis (PEC) process uses synergistic photoelectric technology to catalyze oxidation [21, 22]. Compared with the photocatalytic (PC) system, PEC is more efficient and rapid for sterilization. The traditional photocatalyst is generally supported on the conductive substrate, which serves as the photoanode. The additional potential bias is used as the external driving force to realize the rapid separation of the photogenerated electrons from the conduction to the external circuit, thus fundamentally solving the problem of electron–hole recombination in photolithography production [23, 24]. Due to its fast reaction speed, low energy consumption, simple operation, environmental protection and other characteristics, the water splitting of hydrogen production in water using PEC materials has attracted significant attention [25]. The comparative study of An's group using titanium dioxide nanotubes as photoelectric anodes powerfully demonstrates the broad application of photoelectric anodes in the technical field of antibiotic applications [26, 27].

As an essential part of photo-electrocatalysis, the selection and design of photoanode materials should be taken into consideration [28]. Sulfides are widely used in electrolytes due to their excellent ionic conductivity and good mechanical properties [29]. The PEC over MoS_2 catalyst can produce a variety of ROS such as $^1O_2$, ·OH and $\cdot O_2^-$ under visible light irradiation [30]. These reactive oxygen species make a substantial leap in their ability to kill bacteria by attacking their cell membranes oxidizing proteins and DNA [31–33]. Bacteria are unlikely to develop resistance to ROS due to their high oxidation properties and universality [34]. However, the photogenic electron–hole pairs generated by MoS_2 excitation under visible light are very easy to recombine, which hinders its application in the field of antibacterial. As another transition metal sulfide, single-crystalline Ni_3S_2 is an excellent metal conductor with a room-temperature resistivity of 1.8×10^{-5} Ω·cm [35]. Previous studies have shown that the electrochemical properties of Ni_3S_2 can be significantly improved by combining with other metallic materials to form hybrid heterostructures [36]. Wang et al. [37] reported that the hierarchical core/shell Ni_3S_2@MoS_2 electrode exhibited abundant porosity to promote the electrochemical reaction with fast ions/electrons transportation and improved cyclic retention. This unique core/shell nanostructure may be applied and developed in the field of photocatalytic sterilization. However, Feng et al. reported the heterostructured $NiSe_2$/$MoSe_2$ electronic modulation for efficient electrocatalysis in urea-assisted water splitting reaction [38–40]. Schindra's group reported that MoS_2/α-$NiMoO_4$ nanoneedles with powerful evidence could be used as photocatalytic antibacterial agents convincingly [41]. It provided us with the possibility that Ni_3S_2@MoS_2 can combine their advantages and be used as a photoelectron-catalytic antibacterial agent.

Inspired by the above discussions, nickel foam was selected as the substrate in this work due to its excellent electrical conductivity. Ni_3S_2@MoS_2 core/shell nanostructure was directly grown on the surface of nickel foam by hydrothermal method. It can be used as a photoanode material to react with water molecules and oxygen in the system to activate molecular oxygen to produce ROS,

completely destroying antibiotic-resistant *E. coli* within 25 min. The separation and transfer ability of Ni_3S_2@-MoS_2 heterostructure carriers can effectively improve the inactivation ability of bacteria and can be evaluated by electrochemical impedance spectroscopy (EIS) and photocurrent tests. A series of biological monitoring of bacteria further proved that ROS attacks bacteria during the program in the PEC process. We herein attempt to develop a systematic approach to understand bacterial inactivation mechanisms of PEC and discuss the intracellular enzymatic defensive activities.

2 Experimental

2.1 Catalyst preparation

Photocatalyst Ni_3S_2@MoS_2 was synthesized by hydrothermal method. In the preliminary preparation of the experiment, the surface of soaked nickel foam is cleaned with 5% HCl and acetone to remove any oxide layer that may exist on the surface. The mixed solution was prepared by dissolving 100 mg P123 (a kind of triblock copolymer, $HO(CH_2CH_2O)_{20}(CH_2CH(CH_3)O)_{70}(CH_2CH_2O)_{20}H$), 45
mg sodium molybdate and a certain amount of thioacetamide (TAA, C_2H_5NS) in 30 ml deionized water. The obtained mixed solution was transferred to a high-pressure hydrothermal reaction kettle lined with PTFE, and the pre-treated 2 cm^2 nickel foam was completely immersed in the reaction solution. The autoclave was closed, and the reaction was performed at 210 °C for 24 h in the oven. After the autoclave cooled to room temperature, the sample was washed with deionized water three times and then dried for 12 h in a 60 °C oven. After drying, the samples were heated to 400 °C for 2 h in a tubular furnace with hydrogen and argon mixture (5:95:1 in vol%) at a rate of 10 °C·min^{-1}. The TAA amounts were adjusted as 30, 45 and 60 mg and labeled as NM-1, NM-2 and NM-3, respectively. TAA-free samples were prepared as the control group.

2.2 Activation of antibiotic-resistant *E. coli*

The antibiotic-resistant *E. coli* was provided by the China Centre of Industrial Culture Collection (CICC 10665). Preparation of activating antibiotic-resistant *E. coli*: The strains stored at − 20 °C were activated to 10 ml LB lactose medium, shaking culture at 200 r·min^{-1} for 12 h at 37 °C, then taken centrifugation at 4000 r·min^{-1} for 10 min, washed with ultra-pure water for three times and suspended again to obtain suspension of antibiotic-resistant *E. coli*.

2.3 Reaction apparatus

In this work, a piece of nickel foam on which surface covered with a highly oriented Ni_3S_2@MoS_2 nanotube array (size: 10 mm × 20 mm) was used as the photoanode. The platinum electrode was used as the counter electrode. PC, electrochemical (EC) and PEC inactivation experiments were carried out in a 60-ml dual-electrode photochemical reactor with 0.1 M phosphate buffer electrolyte, + 1.50 V anode bias potential quartz window.

2.4 In vitro photoelectric-induced antibacterial tests

The target strain used in this work was E*scherichia coli* with multiple antibiotic resistance. The bactericidal effect of modified material was evaluated by observing whether the survival rate of bacteria was significantly reduced before and after the PEC reaction with Ni_3S_2@MoS_2 as a photoanode. Firstly, the bacteria were activated in LB medium and shaken under a 37 °C constant temperature shaker for 24 h. PC, EC and PEC reactions were performed for 25 min at 18 W visible light (the LED spectrum in Fig. S1, light intensity is 409.09 W·m^{-2}) irradiation and + 1.5 V additional bias, and 25 μL samples were taken every 5 min for plate coating. After that, the petri dish was placed in a biochemical incubator and cultured for 24 h at a constant temperature of 37 °C. The plate counting method was used to count colony-forming units and compare the antibacterial effect. All experiments were repeated three times to ensure data stability.

2.5 Cytotoxicity tests

Methyl thiazolyl tetrazolium (MTT) assay was used to co-culture the test sample with the target cell HEK293T to detect whether the catalyst had biotoxicity to HEK293T cells. Crushed photoanode material and processed by ultrasonic. Then, 0.1 and 0.2 mg·ml^{-1} samples were co-cultured with HEK293T cells for 24 h to observe the cell viability. MTT colorimetry was used to evaluate cell viability before and after co-cultivation. The absorbance of the well was measured by immunosorbent assay using a microplate reader at OD = 560 nm (calibration was performed at OD = 630 nm). The test needs to be repeated several times for all samples to ensure the stability of the experiment.

2.6 ROS tests

ROS generation was measured by an electron paramagnetic resonance (EPR) spectrometer. The chemical probe 5,5-dimethyl-1-pyrrolidine N-oxide (DMPO) acted as a spin trap. DMPO (10 mM) was dispersed in methanol to detect $\cdot O_2^-$, and ·OH could be detected in the aqueous dispersion

of DMPO. The ROS vibration signals of different sample materials as photoanode materials for PEC reaction were compared. The ROS scavenger experiment was carried out by adding the corresponding trapping reagent in the photocatalytic reactor. Isopropanol (0.5 mM), oxalic acid (0.5 mM), 4-hydroxy-2,2,6,6-tetramethylpiperidine-1-oxy (TEMPOL, 2 mM) and EDTA (II) solution (0.5 mM) were used as scavengers of ·OH, h^+, $\cdot O_2^-$ and H_2O_2, respectively.

3 Results and discussion

3.1 Characterization of Ni_3S_2@MoS_2

With miniaturization, the fraction of free surfaces increases, which has dominated influence on the total mechanical properties of the material.

In this work, nickel foam was used as the substrate material and Ni source, TAA was used as the S source, and sodium molybdate was used as the Mo source. Figure 1 is the flowchart of the preparation process. Ni_3S_2@MoS_2 core/shell heterostructure nanorod array was prepared by hydrothermal method. According to Reaction (1), active species of S are isolated and released from TAA at the initial stage of the reaction. Then, in the nucleation procedure, the S ions reacted with Ni foam to form Ni_3S_2 nanoparticles (Reaction (2)), and the MoO_4^{2-} released from sodium molybdate forms MoS_2 nanoparticles according to Reaction (3). Ni_3S_2 nanoparticles deposited on the surface of nickel foam were induced to grow into nanorods through a complex directional growth process. After the successful growth of nanorods, they could be used as the skeleton to induce the preferential deposition of MoS_2 nanosheets. It is worth noting that Ni foam plays an important role during the reaction, which not only acts as

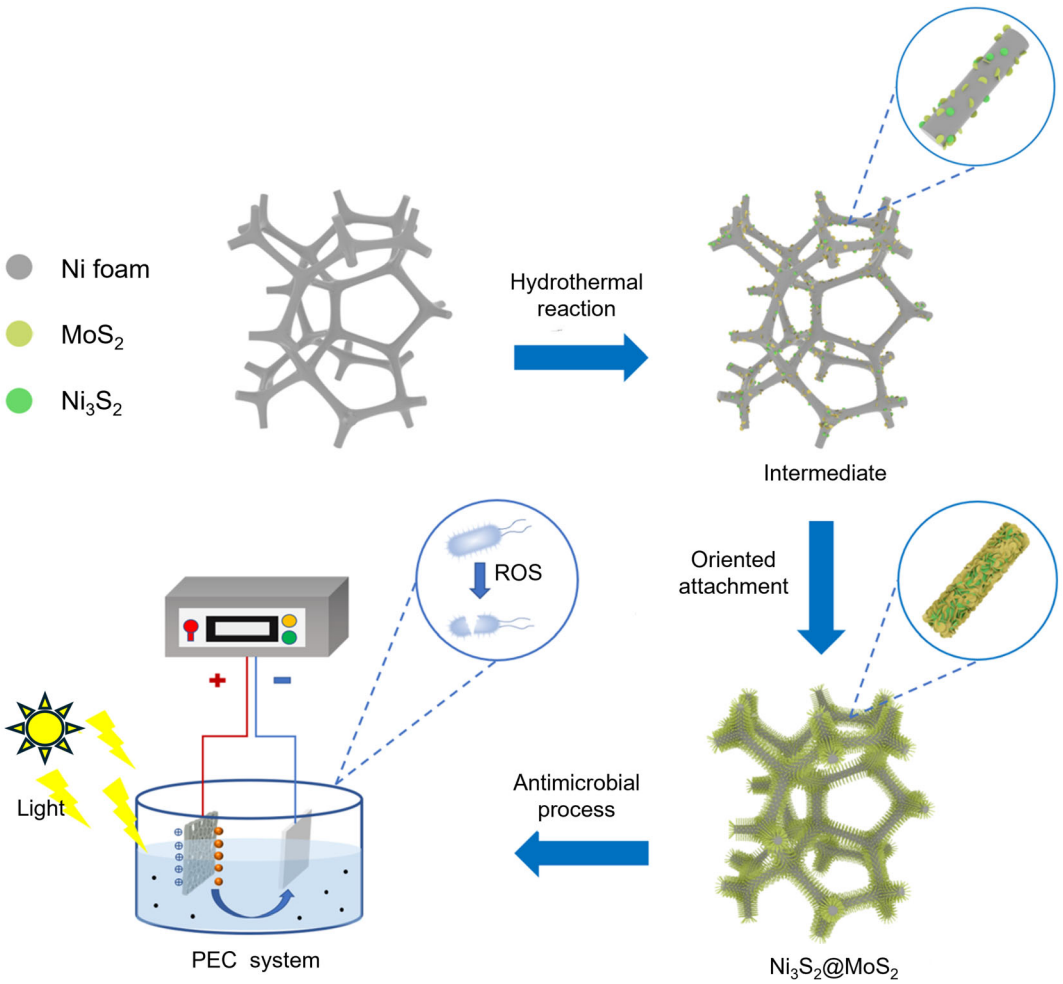

Fig. 1 Flowchart of Ni_3S_2@MoS_2 core/shell array synthesis on nickel foam surface by hydrothermal method and schematic diagram of reaction apparatus

the substrate for the growth of Ni_3S_2@MoS_2 nanorods but also provides Ni source to form Ni_3S_2.

$$NH_2CSNH_2 + H_2O \rightarrow 2NH_3 + 2H_2S + CO_2 \quad (1)$$

$$3Ni + 2H_2S \rightarrow Ni_3S_2 + 2H_2 \quad (2)$$

$$MoO_4^{2-} + 3H_2S \rightarrow MoS_2 + 3H_2 + SO_4^{2-} \quad (3)$$

The morphology of the as-synthesized Ni_3S_2@MoS_2 composite was observed by scanning electron microscopy (SEM) and transmission electron microscopy (TEM) techniques. SEM images of Ni_3S_2@MoS_2 nanorods at different magnifications are shown in Fig. 2a, b. The surface of the initially smooth nickel foam is densely covered with neat nanorods with diameters of 80–100 nm and lengths of 2 μm which grow orderly and vertically on the substrate. The hierarchical core/shell heterostructure was demonstrated under a close SEM observation (Fig. 2b); the MoS_2 nanosheets uniformly covered the Ni_3S_2 nanorods. Compared with bare Ni foam and samples, NM-0, NM-1, NM-2 and NM-3 had better Ni_3S_2 nanorods growing and more MoS_2 nanosheets interconnection, which could provide great active sites and accelerated photoelectrochemical reactions, leading to higher sterilizing efficiency. The core/shell structure of Ni_3S_2@MoS_2 nanorods was further investigated by high-resolution transmission electron microscopy (HRTEM). A TEM image of a single Ni_3S_2@MoS_2 nanorod is depicted in Fig. 2c, a layer of MoS_2 nanosheets wrapped Ni_3S_2 nanorod with a thickness of 10 nm. HRTEM result obtained from the yellow square area is shown in Fig. 2d. The lattice spacing is 0.62 and 0.24 nm, respectively, corresponding to the (002) crystal plane of MoS_2 and (011) crystal plane of Ni_3S_2. In addition, the energy-dispersive

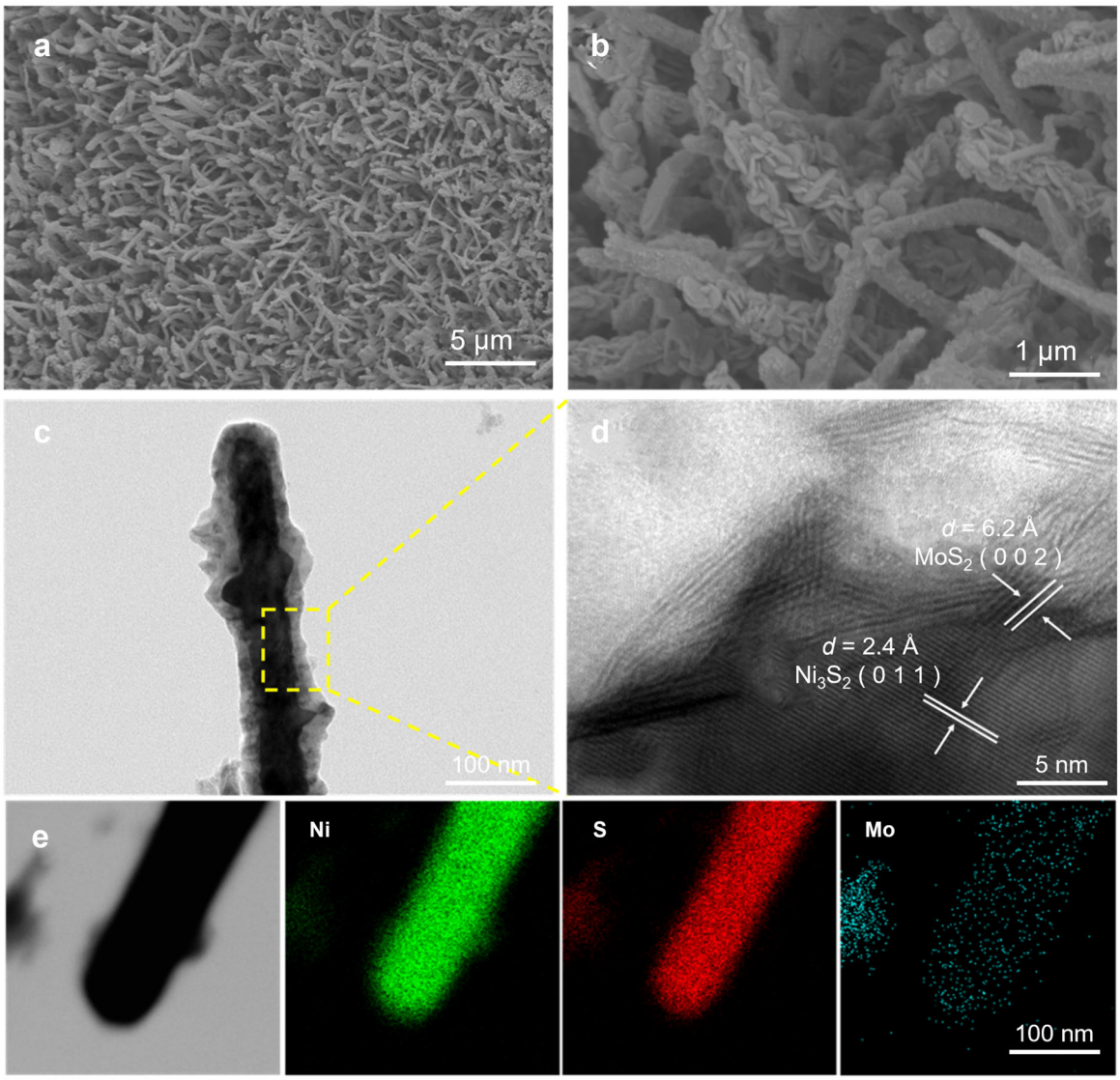

Fig. 2 Morphology characterization of Ni_3S_2@MoS_2 nanorod arrays: **a**, **b** SEM images of Ni_3S_2@MoS_2 nanorod arrays; **c**, **d** HRTEM images and **e** EDS mappings of Ni_3S_2@MoS_2 nanorod

X-ray spectrometry (EDS) analysis confirmed the composition of Ni_3S_2@MoS_2 nanorod and Ni, S and Mo elements were uniformly distributed on the single nanorod (Fig. 2e). The results demonstrated that the as-synthesized Ni_3S_2@MoS_2 nanorod was a hierarchical core/shell heterostructure that may enhance the photoelectrochemical performance.

The crystalline structure of the as-prepared Ni_3S_2@-MoS_2 composite was further characterized by X-ray diffraction (XRD) (Fig. S2a). Three strong peaks at 44.4°, 51.8° and 76.3° are assigned to the (111), (002) and (022) lattice planes of the metallic Ni foam substrate (JCPDS No. 10-2279). The other strong diffraction peaks at 21.8°, 31.1°, 37.8°, 44.4° and 55.2°correspond to the (101), (110), (003), (202) and (122) planes of Ni_3S_2 (JCPDS No. 30-0863). The MoS_2-related peaks are located at 14.5° and 33.1°, attributed to the (003) and (101) planes, respectively (JCPDS No. 86-2308). This result was quite consistent with HRTEM analysis, indicating that the Ni_3S_2@MoS_2 composite prepared through the hydrothermal method has a good crystal phase and high purity. According to the solid UV absorption spectrum (Fig. S2b), the composite material Ni_3S_2@MoS_2, compared with the pure nickel foam and Ni_3S_2, broadens the range of strong absorption bands and has stronger absorption of visible light. It can realize the efficient utilization and absorption of the external light source and contribute to the material to produce more reactive oxygen free radicals.

In addition, the surface chemical valence state of Ni_3S_2@MoS_2 and Ni_3S_2 was measured by X-ray photoelectron spectroscopy (XPS). The full survey spectrum of Ni_3S_2@MoS_2 and Ni_3S_2 in Fig. 3a indicated that in the presence of Ni, S and Mo, the peaks at 873.7 and 856.0 eV in the Ni 2p high-resolution spectrum were ascribed to Ni $2p_{1/2}$ and Ni $2p_{3/2}$, respectively, which were ascribed to the coexistence of Ni^{2+}an Ni^{3+} species, whereas the two satellite peaks at 879.9 and 861.2 eV were attributed to Ni–O categories, which were caused by the superficial oxidation of the sample. The nanosheets composite architecture of Ni_3S_2@MoS_2 exhibited a characteristic peak at 870.6 eV corresponding to Ni–S bond, which was shifted in comparison with Ni_3S_2 (870.3 eV), indicating that the strong electronic interactions between Ni_3S_2 and MoS_2 resulted in the charge redistribution on their interfaces. Additionally, the bonding energy at 228.8 and 232.2 eV of Mo $3d_{5/2}$ and Mo $3d_{3/2}$ could be assigned to Mo^{4+}. The peak at 226.0 eV could be distributed to S 2s, which suggested the formation of Ni–S and Mo–S bonding [42], while the peak at 235.5 eV corresponded to Mo^{6+}, indicating that the surface of MoS_2 was oxidized due to contact with air [43]. The bonding energy at 168.5 eV was the characteristic peak of the S–O bond, which was attributed to high oxidation at the edge. In addition, two peaks of Ni_3S_2@MoS_2 at 161.4 and 162.6 eV were two characteristic peaks of S $2p_{3/2}$ and S $2p_{1/2}$, respectively, which could be ascribed to the S^{2-} of metal sulfur species [44]. However, these two peaks were shifted negatively migrated compared with Ni_3S_2 (161.8 and 163.0 eV), respectively, indicating additional electrons transfer to S atom in Ni_3S_2@MoS_2.

3.2 Photoelectric-induced antibacterial activity of Ni_3S_2@MoS_2

Figure 4a shows the disinfection effects of *E. coli* exposed to the nickel foam, Ni_3S_2 and different proportions of Ni_3S_2@MoS_2 under visible light illumination. As could be seen from Fig. 4a, the photoactive sterilization effect of NM-3 was obviously better than others under similar concentration and culture conditions. The viability of AR *E. coil* through various inactivation methods is shown in Fig. 4b. There is rarely an inactivation effect under PC and EC conditions after 40 min treatment, while the inactivation efficiency achieved 100% in the PEC process within 25 min. The significant enhancement of inactivation efficiency was attributed to the strongly inhibited recombination of photogenerated electron–hole pairs in the PEC system. In contrast, this suppression would not occur in the PC system. In addition, the Gram-positive bacteria represented by *Staphylococcus aureus* (*S. aureus*) and another common Gram-negative bacterium *Pseudomonas Aeruginosa* (*P. aeruginosa*) were used to test whether the antibacterial effect of Ni_3S_2@MoS_2 on other bacteria is universal. The experimental results in Fig. 4c directly illustrate the antibacterial ability of Ni_3S_2@MoS_2 not only effects on *E. coli*, but also has an efficient antibacterial effect on other bacteria under PEC treatment. Among them, compared to Gram-negative bacteria, Gram-positive bacteria are more resistant, probably due to the presence of a large number of peptidoglycan special structures in their cell wall structure.

3.3 Cell damage of *E. coli* treated by Ni_3S_2@MoS_2

Morphological changes of AR *E. coli* before and after PEC sterilization can be observed by SEM and TEM. As shown in Fig. 5a, c, before the PEC treatment, the morphology of AR *E. coli* was short and full, and the structure of AR *E. coli* was complete. As can be seen from Fig. 5b, d, after the treatment with external bias pressure and visible light irradiation, holes appeared on the outer membrane surface of bacteria. Finally, the outer membrane of cells broke, the original intracellular substances inside the bacteria leaked, and the shape of bacteria was completely destroyed. The results showed that the AR *E. coli* could be killed effectively using Ni_3S_2@MoS_2 material as photoanode material

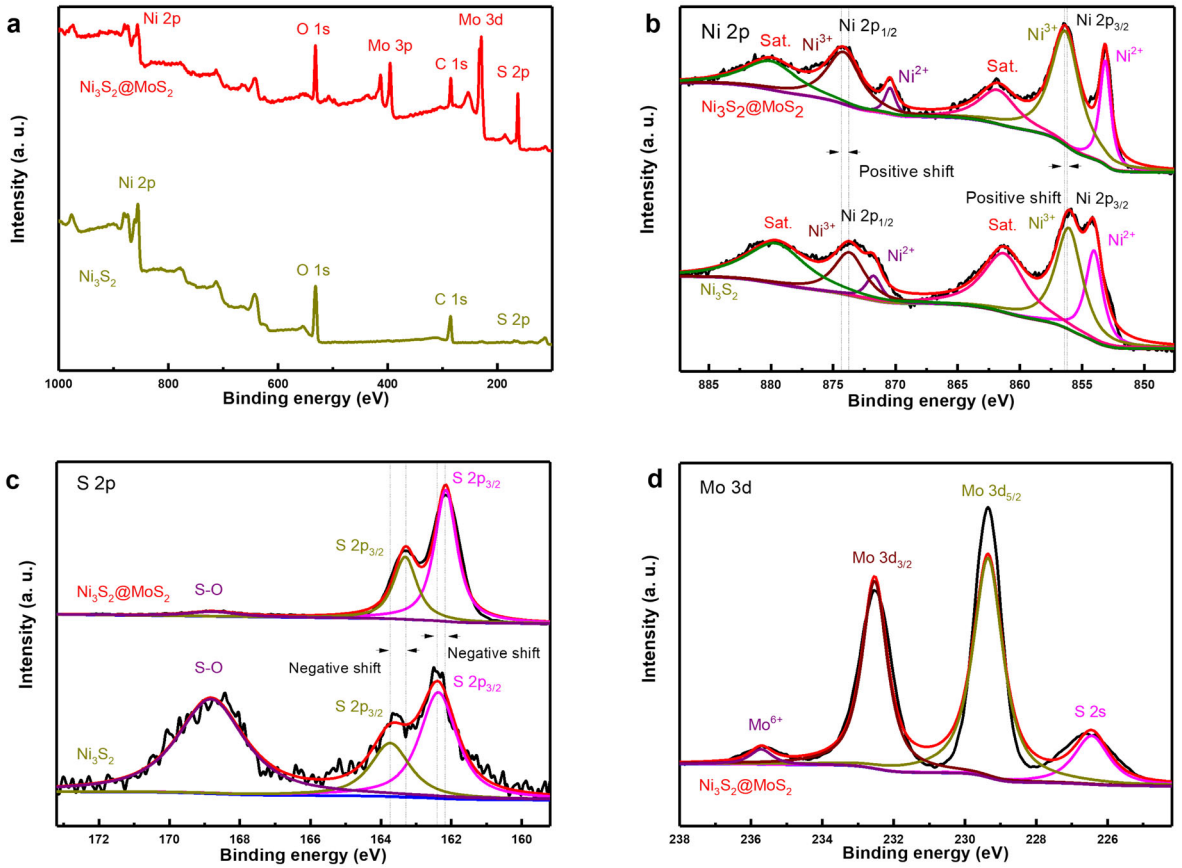

Fig. 3 XPS spectra of Ni_3S_2@MoS_2: **a** XPS spectra and corresponding high-resolution spectra of **b** Ni 2p, **c** S 2p and **d** Mo 3d

for PEC operation. The bacterial morphology was completely consistent with the antibacterial test results.

In addition to the process of the plate, the laser copolymer was also studied, and the effect of the laser copolymer microscope on the sterilization of Ni_3S_2@MoS_2 was further demonstrated. The dye is a PI dye, which can penetrate the damaged bacteria in vitro membrane and mark red fluorescence. The bacteria that emit red fluorescence on the laser confocal microscope can be identified as damaged in the cell membrane, and the fungus is broken. The optical and fluorescence images of AR *E. coli* treated with PI dye and observed by confocal laser microscope at an excitation wavelength of 535 nm are shown in Fig. 5e. Almost no dead AR *E. coli* cells could be observed before Ni_3S_2@MoS_2 treatment. Interestingly, AR *E. coil* cells basically displayed red fluorescence after the PEC process, in which conclusion is consistent with the previous conclusion of bacterial destruction by plate coating.

3.4 Bacterial decomposition and biomolecules leakage

In PEC bacterial inactivation, various ROSs are generated via successive single-electron reductions, producing superoxide (O^{2-}), hydrogen peroxide (H_2O_2) and hydroxyl radical (OH^-) [45], while bacterial superoxide dismutases (SODs) and catalases can enzymatically degrade superoxide and hydrogen peroxide. This mechanism involved the production of hydroxyl radicals and was reported to depend on metabolism-related NADH depletion, the tricarboxylic acid (TCA) cycle, the electron transport chain, damage of iron-sulfur clusters in proteins and stimulation of the Fenton reaction [46]. Metabolism in general plays an important role in antibiotic mediated killing, and depending on the conditions, ROS generated by hyperactivation of metabolism are more or less important for killing [47]. ROS are produced as a consequence of the interaction of antibiotics with their classical targets. The increased ROS production which will also effectively contribute to cell killing is further dependent on the presence of ROS defense and repair mechanisms. Due to the formation of ROS in intracellular and extracellular locations, oxidative stress can damage the cell and cause reactions of antioxidant enzymes in bacteria, the most prominent representatives are superoxide dismutase (SOD) and catalase (CAT); their main roles are to carry out catalytic transformation and detoxification of $\cdot O_2^-$ and H_2O_2, respectively, to alleviate damage to bacteria caused by the generation of ROS [48].

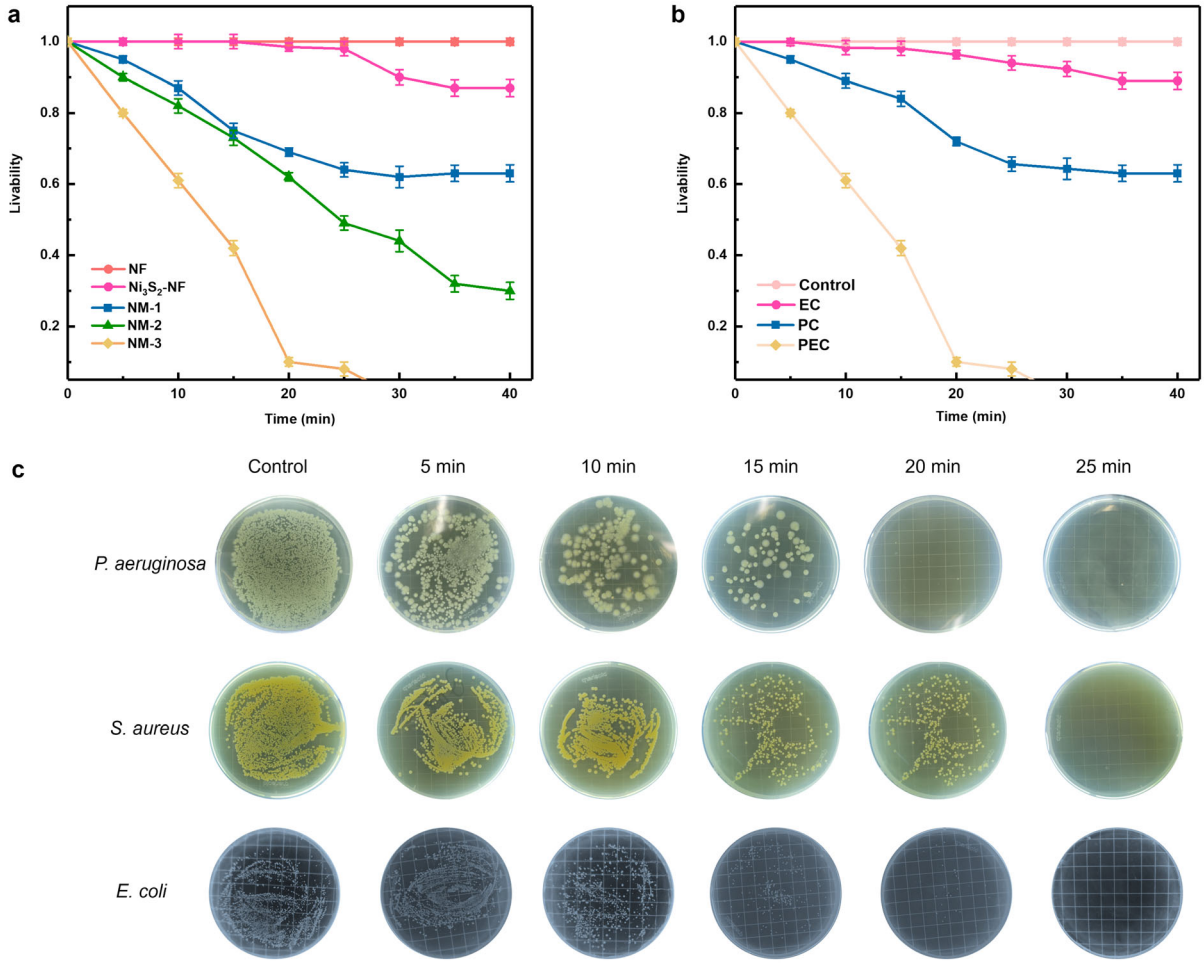

Fig. 4 **a** Survival curves of Escherichia coli under different photoanode samples over time; **b** different conditions under PEC, PC and EC for 40 min; **c** survived colony growth of *Pseudomonas Aeruginosa*, *Staphylococcus Aureus* and *Escherichia coli* treated by Ni_3S_2@MoS_2 at different time

Therefore, the physiological changes of bacteria under ROS attack were evaluated by detecting the changes in SOD and CAT enzyme activities during PC, EC and PEC reactions. And the results are shown in Fig. 6. In the process of PC and EC, the enzyme activities of the two enzymes did not change significantly with the progress of the reaction, which proved that the two enzymatic reactions in bacteria were not greatly affected under the two catalytic modes. When the reaction started, the enzyme activities of both enzymes decreased and continued to decline in the subsequent process. According to relevant reports, when bacteria are subjected to the oxidative attack of reactive oxygen free radicals, SOD and CAT will be damaged by oxidation, resulting in the loss of enzyme activity and eventually leading to protein fracture and protein hydroxyl derivatives [49]. At the initial stage of the reaction, the rapidly increasing ROS level in bacterial cells exceeds the catalytic decomposition threshold range of SOD and CAT, leading to decreased SOD and CAT activities. With the loss of SOD and CAT activities, the reaction accelerates ROS accumulation, thus leading to the loss of bacterial biological activity.

Bradford analysis method is widely used to explore the degree of protein degradation. Table 1 shows the degree of protein degradation after three different catalytic methods under visible light irradiation. The percentage of protein degradation also varies significantly according to the catalytic method such as electrocatalysis (EC), PC and PEC were 7%, 18.3% and 51.88%, respectively. According to the degradation results presented in Table 1, in PEC catalysis using Ni_3S_2@MoS_2 as photocatalytic anode material, more reactive oxygen groups are generated, and these reactive oxygen groups play a role in protein degradation from gas to middle and high waist. In amino acids, the attack of active sites of amino and carboxyl functional groups and the rupture of peptide bond links may be important causes of protein degradation and bacterial death. Gel protein electrophoresis was used to analyze the

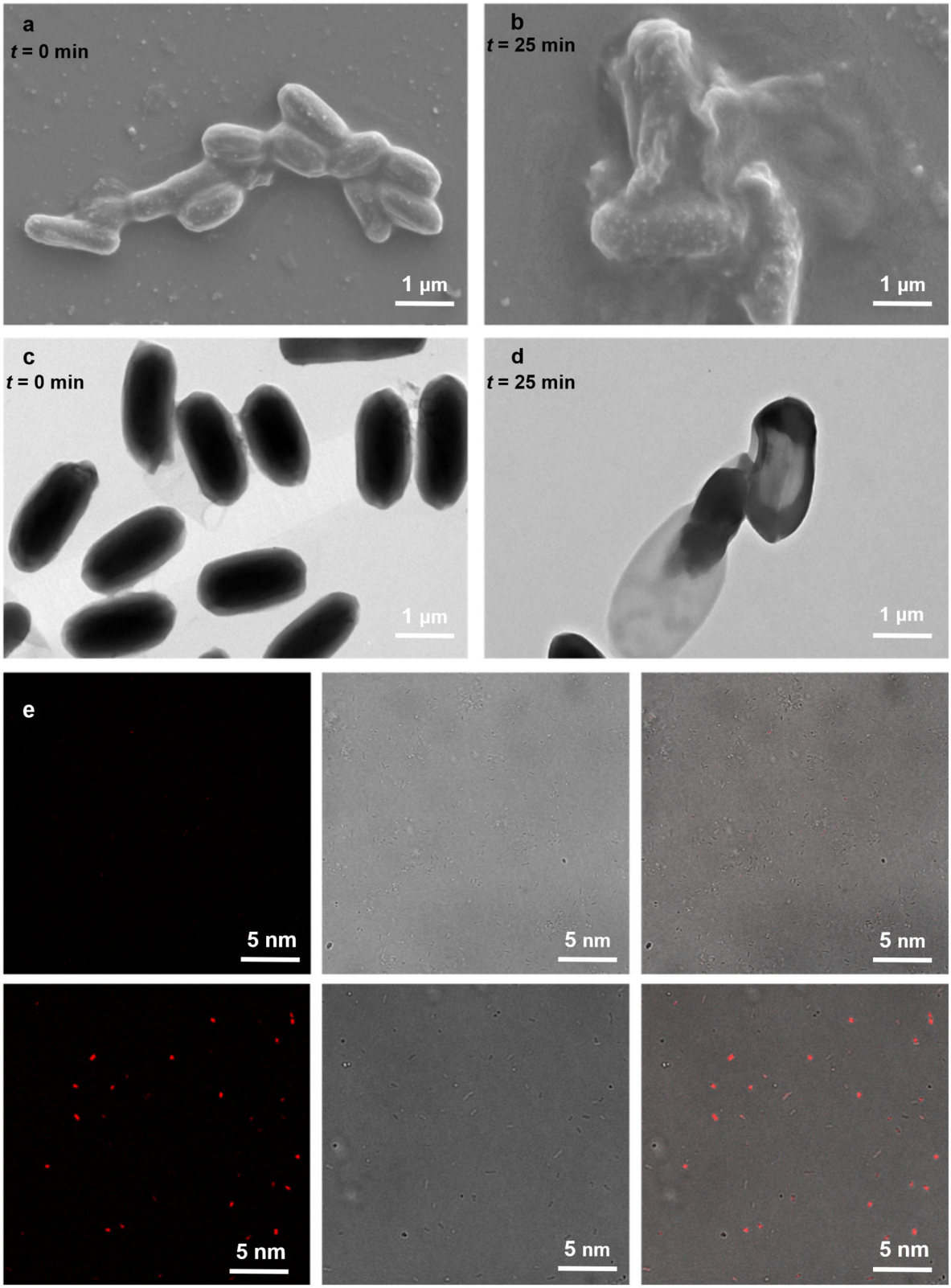

Fig. 5 SEM images of PEC inactivation of AR *E. coli:* t = **a** 0, **b** 25 min; TEM images of PEC inactivation of AR *E. coli:* t = **c** 0, **d** 25 min; **e** fluorescent images, optical images and double-channel overlay antibiotic-resistant AR *E. coli* before and after PEC treatment with Ni_3S_2@MoS_2

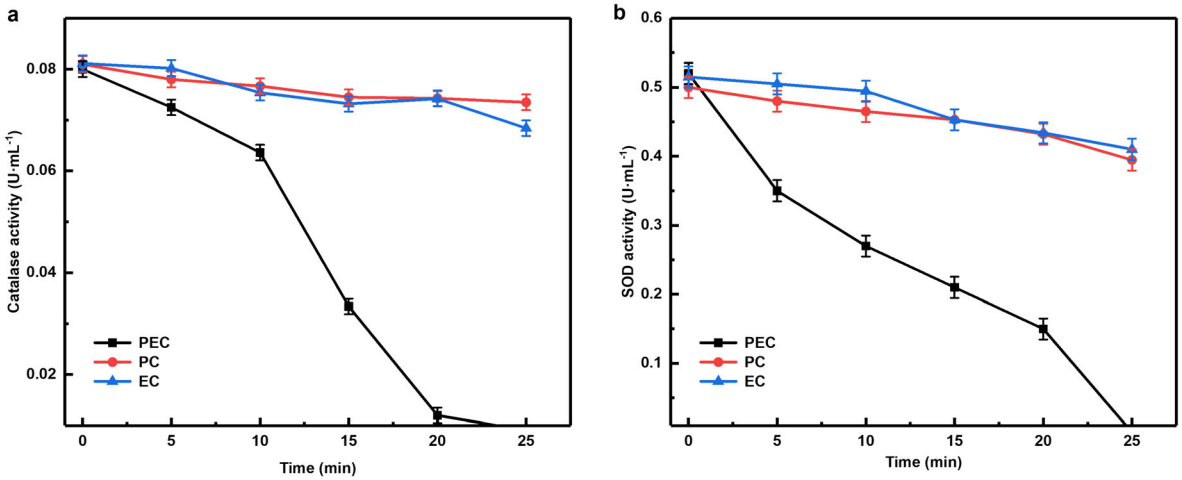

Fig. 6 Activities changes of **a** SOD and **b** CAT with different treatment time

Table 1 Protein degradation rate under different sterilization treatments

Sample	Absorbance at 595 nm
Control	0.916 ± 0.004
EC	0.849 ± 0.002
PC	0.748 ± 0.004
PEC	0.441 ± 0.005

protein damage caused before and after the PEC reaction under visible light irradiation, as shown in Fig. S3. Compared with the protein gel electrophoresis bands in the control group, the bands became significantly darker after PEC treatment, and the protein damage was severe. In the process of protein degradation, ROS produced by visible light irradiation of photocatalyst will attack the C5/C6 positions of nitrogen-containing bases (such as thymine, adenine, guanine), resulting in sugar/strand breaks and base loss [50].

3.5 Damage of DNA

Although the damage and leakage of proteins will cause harm to bacteria, such damage is not irreversible. Under specific conditions and environments, bacteria can even repair and regenerate proteins [51]. In contrast, DNA damage is more intuitive and irreversible. Thus, the total DNA of antibiotic-resistant *E. coli* before and after the PEC reaction with Ni_3S_2@MoS_2 was further monitored to evaluate the activity of *E. coli* (Fig. 7a). When the total amount of DNA in bacteria was extracted, the concentration of DNA decreased within the first 10 min of the reaction, demonstrating the damage of genetic material caused by ROS oxidation attack on DNA. These results can also be confirmed by the gel electrophoresis method (Fig. 7b).

According to previous studies, hydroxyl radicals play a key role in the lethal oxidative damage attack on DNA. The abstractions and addition reactions induced ·OH can produce carbon-centered sugar radicals and -OH or -H adduct radicals of heterocyclic bases. In order to verify the damage of bacterial DNA during PEC treatment, two reference genes of frdD and acrB were marked, and the bacterial fluid before and after reaction for 20 min was selected for PAGE analysis (Fig. 7c). When the reaction time was 0, two bands of frdD and acrB were observed clearly. However, the bands of these two marker genes could not be found in the bacterial fluid samples 20 min after the reaction, which proved that the PEC disinfection method using modified Ni_3S_2@MoS_2 materials as photoelectric anode effectively destroyed these two reference genes within 20 min.

3.6 Cytotoxicity tests

Whether the photoelectrical sterilization catalyst prepared in this paper has cytotoxicity is of great significance for its application in biomedical science. MTT assay was used to co-culture the test sample with the target cell HEK293T to detect whether the catalyst had biotoxicity to HEK293T cells [52]. Crushed photoanode material and processed by ultrasonic. The chosen 0.1 and 0.2 $mg{\cdot}ml^{-1}$ samples were co-cultured with HEK293T cells for 24 h. MTT colorimetry was used to evaluate the cell viability before and after co-cultivation, and the analysis results are shown in Fig. S4. After adding samples of different concentrations, the cell survival rates began to decline from 100% to 93.35% (0.1 $mg{\cdot}ml^{-1}$), 91.29% (0.2 $mg{\cdot}ml^{-1}$). According

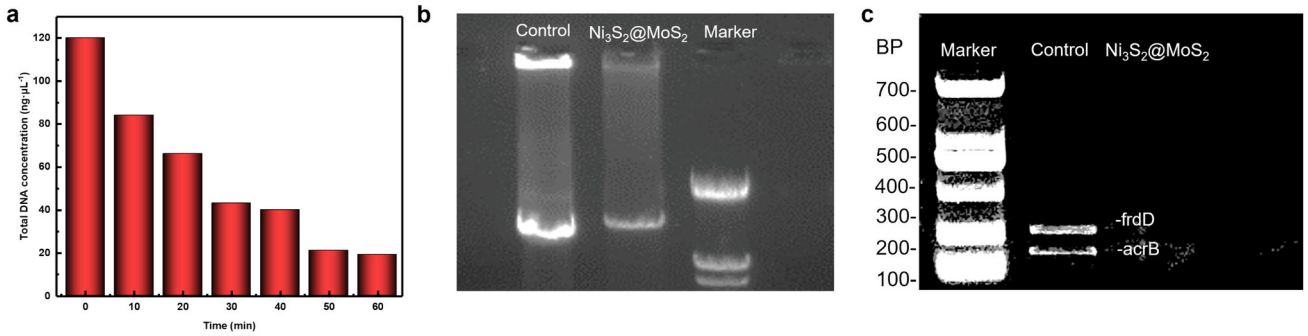

Fig. 7 **a** Changes of total DNA; **b** gel electrophoresis image of total DNA in Ni_3S_2@MoS_2 disinfection process; **c** changes of frdD and acrB labeled genes during PEC disinfection

to the test results, the addition of Ni_3S_2@MoS_2 did not significantly reduce the biological activity of the cells. The above experiment concluded that Ni_3S_2@MoS_2 has good photocatalytic antibacterial performance and good biocompatibility, which was also mentioned in our group's previous work.

3.7 Discussion on antibacterial mechanism

To inspect the feasibility of repetitively using Ni_3S_2@MoS_2 electrodes for the PEC process, the AR *E. coli* disinfection experiments were repeated with recycled Ni_3S_2@MoS_2 electrodes. After each experiment, the Ni_3S_2@MoS_2 electrode was removed from the electrode clip and washed with deionized water three times before starting the next run. The disinfection results of using recycled Ni_3S_2@MoS_2 in the PEC system are presented in Fig. S5. These results showed that after repeated tests three times, the Ni_3S_2@MoS_2 electrode still had an excellent bacteriostatic performance. The morphology and surface state of Ni_3S_2@MoS_2 photoelectrode do not have a significant change after antibacterial activity test (Fig. S6). Compared with the defects of traditional nanoparticle photocatalysts dispersed in water, it was difficult to recycle and may cause some pollution to the environment. The Ni_3S_2@MoS_2 electrode was reusable and environmentally friendly.

To further investigate the photoelectrochemical catalytic reaction of as-prepared Ni_3S_2@MoS_2 and Ni_3S_2, DMPO was employed as a spin trap for the hydroxyl radical and superoxide anion, respectively, and 4-oxo-TEMP to detect singlet oxygen [53]. As a spin trap, 4-oxo-TEMP itself is EPR silent, but it can specifically capture $^1O_2$ to yield a nitroxide radical, TEMPONE, which has an observable and stable EPR spectrum [54]. EPR technology was used to identify the active radicals responsible for the antibacterial process using TEMP and DMPO as the spin catcher [55, 56]. As seen in Fig. 8a, the signal of DMPO-·O_2^- was clearly observed in the Ni_3S_2@MoS_2/PEC system, and the characteristic signal of three lines with the same intensitiy was attributed to TEMP-$^1O_2$ (Fig. 8b). The $^1O_2$ as a secondary species was generated via Reaction (4), which suggested that ·O_2^- was the dominant reactive oxidation species of the PEC system.

$$\cdot O_2^- + 2H_2O \rightarrow^1 O_2 + H_2O_2 + 2H^+ \quad (4)$$

2,2,6,6-tetramethyl-4-piperidinol-N-oxyl (TEMPO), generated through the reaction between TEMP and $^1O_2$, is used as a probe for e^-/h^+. As shown in Fig. 8c, the e^-/h^+ signal of the PEC system verified that e^-/h^+ also contributed to the enhancement of PEC efficiency (Reaction (5)). The presence of signals of DMPO-·OH and DMPO-·OOH demonstrated in Fig. 8d indicated that both ·OH and ·OOH were generated by catalysts after PEC treatment (Eq. (6)).

$$\text{Cat.} + h\nu \rightarrow e^- + h^+ \quad (5)$$

$$H_2O_2 \rightarrow 2\cdot OH \quad (6)$$

It is worth noting that the free radicals mentioned above were detected in both Ni_3S_2@MoS_2/PEC and Ni_3S_2/PEC systems under the same experimental conditions. Still, the intensity of the signal in the Ni_3S_2@MoS_2/PEC system was much stronger than that of the Ni_3S_2/PEC system, indicating that the Ni_3S_2@MoS_2 catalyst could reach better performance and was more suitable for sterilization.

By measuring the photocurrent response of the nickel foam (NF), Ni_3S_2, MoS_2 and Ni_3S_2@MoS_2 under visible light irradiation, reflecting the separation efficiency of photogenerated electron–hole pairs of these four materials, are observed. The photocurrent is caused by the energy excitation of visible light, which leads to the electron energy level transition in the internal structure of photocatalyst, resulting in the separation of electron–hole pairs, and then the diffusion of free charge on the surface of photocatalyst and in an electrolyte solution. By comparing the photocurrent response curves of the four materials, a higher photocurrent response can be obviously observed in

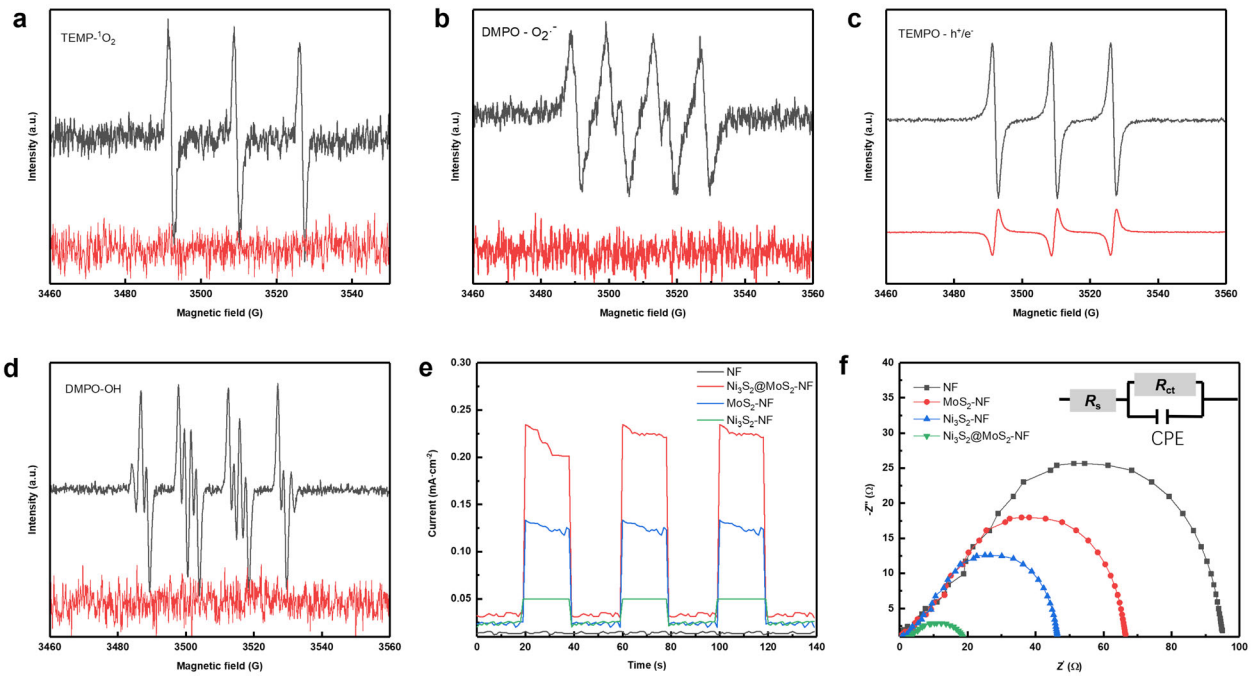

Fig. 8 EPR spectra of **a** $\cdot O_2^-$, **b** $^1O_2$, **c** h^+, e^- and **d** ·OH of Ni_3S_2@MoS_2 and Ni_3S_2; **e** transient photocurrent responses and **f** EIS spectra of nickel foam (NF), Ni_3S_2, MoS_2 and Ni_3S_2@MoS_2

Fig. 8e, which proves that the modified material has the strongest ability to generate photogenerated electron–hole pairs under the best response effect for visible light. Light in EIS photocatalytic materials is studied in electron–hole mobility and compound function. In general, the smaller radius of the arc contributed to a better charge transfer rate, which proves that the electrochemical properties of modified materials are better (Fig. 8f). Due to the porous sheet shell, the heterostructure Ni_3S_2@MoS_2 nanorod arrays also possess a high Brunauer–Emmett–Teller (BET) surface area of 38.26 $m^2 \cdot g^{-1}$ with a pore volume of 0.65 $m^3 \cdot g^{-1}$, as shown in Fig. S7, which is beneficial for the transport and diffusion of electrolyte ions during the charge–discharge process of supercapacitors. All those tests prove that after the Ni_3S_2 and MoS_2 are combined, the composite material has a higher interfacial charge transfer rate and a more thorough pair separation rate, further improving the bactericidal effect Ni_3S_2@MoS_2.

The antibacterial mechanism of Ni_3S_2@MoS_2 is illustrated in Fig. 9. By absorbing the energy generated by visible light, highly separated electron–hole pairs are generated under the action of PEC. After reacting with water and oxygen, a large number of extracellular reactive oxygen species, such as $^1O_2$, $\cdot O_2^-$ and ·OH, are generated. These reactive oxygen species can penetrate bacterial cells, resulting in a rapid rise of intracellular reactive oxygen species in a short time. SOD and CAT in the bacteria are attacked and unable to continue their antioxidant function. At the expected time, the integrity of the bacterial cell membrane is also destroyed. The rupture of bacterial cell membrane and lysis of bacteria can be observed in both scanning and transmission images. The content of protein and DNA was detected, and both protein and DNA were damaged. The synthetic primer was used to specifically label the gene fragment with antibiotic resistance, which was oxidized and eliminated after PEC reaction, proving that this material for PEC antibacterial can not only kill bacteria. Successful elimination of antibiotic-resistance gene fragments can also be achieved.

4 Conclusion

In short, compared with the Ni_3S_2 and MoS_2, Ni_3S_2@MoS_2 had the better photoelectric catalysis performance. Under the condition of external bias voltage and visible light irradiation, the photoanode material prepared in this paper achieved effective inactivation of antibiotic-resistant *E. coli* in 25 min. The photoelectric chemistry experiment shows that compared with other materials, Ni_3S_2@MoS_2 material with Mo atomic site has lower electron transfer resistance and a more thorough electron–hole separation rate, which contributes to the generation of more ROS in the PEC process and improves its sterilization efficiency. The changes in bacterial morphology before and after the reaction were observed by SEM and TEM, and the amount

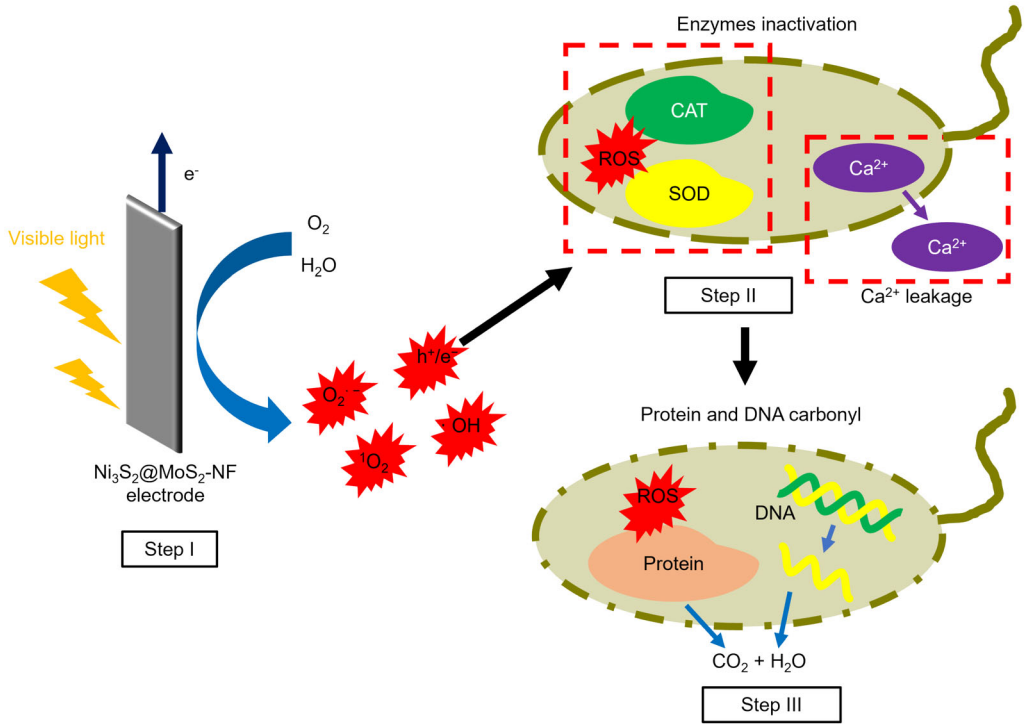

Fig. 9 Schematic illustration of antibacterial mechanism of Ni_3S_2@MoS_2

of ion release, protein degradation rate and DNA degradation rate in the bacteria were monitored, which proved the inactivation of the antibiotic-resistant *E. coli* from multiple perspectives. In conclusion, Ni_3S_2@MoS_2 is a promising photocatalytic material, which can be applied to the decomposition of antibiotic-resistant bacteria in polluted wastewater.

Acknowledgements This work was financially supported by the Fund of AHBMC-AHU Joint Laboratory of Biomedical Material (No. 2022340102000659), the 512 Talent Cultivation Plan of Bengbu Medical College (No. 51201313), the Young Scientist Fund of Bengbu Medical College (No. 2021byyfyyq02) and the Scientific Research Fund of Anhui Provincial Education Department (No. 2023AH040290).

Declarations

Conflict of interests The authors declare that they have no conflict of interest.

References

[1] Martínez JL. Antibiotics and antibiotic resistance genes in natural environments. Science. 2008;321:365. https://doi.org/10.1126/science.1159483.

[2] Guo CS, Wang K, Hou S, Wan L, Lv JP, Zhang Y, Qu XD. H_2O_2 and/or TiO_2 photocatalysis under UV irradiation for the removal of antibiotic resistant bacteria and their antibiotic resistance genes. J Hazard Mater. 2017;323:710. https://doi.org/10.1016/j.jhazmat.2016.10.041.

[3] Povolo VR, Ackermann M. Disseminating antibiotic resistance during treatment. Science. 2019;364:737. https://doi.org/10.1126/science.aax6620.

[4] Ma HK, Zhang LL, Huang XM, Ding W, Jin H, Li ZF, Cheng SK. A novel three-dimensional galvanic cell enhanced Fe^{2+}/persulfate system: high efficiency, mechanism and damaging effect of antibiotic resistant *E. coli* and genes. Chem Eng J. 2019;362:667. https://doi.org/10.1016/j.cej.2019.01.042.

[5] Chen H, Zhang MM. Effects of advanced treatment systems on the removal of antibiotic resistance genes in wastewater treatment plants from Hangzhou, China. Environ Sci Technol. 2013;47(15):8157. https://doi.org/10.1021/es401091y.

[6] Nnadozie CF, Odume ON. Freshwater environments as reservoirs of antibiotic resistant bacteria and their role in the dissemination of antibiotic resistance genes. Environ Pollut. 2019;254: 113067. https://doi.org/10.1016/j.envpol.2019.113067.

[7] Zhang H, Li L, Li QQ, Ma T, Gao JQ, Xue JB, Gao S. Graphitic carbon nitride loaded with bismuth nanoparticles displays antibacterial photocatalytic activity. Rare Met. 2022;41(5):1570. https://doi.org/10.1007/s12598-021-01921-y.

[8] Feng HM, Wang W, Zhang MT, Zhu SD, Wang Q, Liu JG, Chen SG. 2D titanium carbide-based nanocomposites for photocatalytic bacteriostatic applications. Appl Catal B: Environ. 2020;266:118609. https://doi.org/10.1016/j.apcatb.2020.118609.

[9] Tang YN, Sun H, Qin Z, Yin SY, Tian LM, Liu ZN. Bioinspired photocatalytic ZnO/Au nanopillar-modified surface for enhanced antibacterial and antiadhesive property. Chem Eng J. 2020;398:125575. https://doi.org/10.1016/j.cej.2020.125575.

[10] Ferro G, Guarino F, Cicatelli A, Rizzo L. β-lactams resistance gene quantification in an antibiotic resistant *Escherichia coli* water suspension treated by advanced oxidation with UV/H_2O_2. J Hazard Mater. 2017;323:426. https://doi.org/10.1016/j.jhazmat.2016.03.014.

[11] McKinney CW, Pruden A. Ultraviolet disinfection of antibiotic resistant bacteria and their antibiotic resistance genes in water

and wastewater. Environ Sci Technol. 2012;46:13393. https://doi.org/10.1021/es303652q.
[12] Abou Saoud W, Kane A, Le Cann P, Gerard A, Lamaa L, Peruchon L, Brochier C, Bouzaza A, Wolbert D, Assadi AA. Innovative photocatalytic reactor for the degradation of VOCs and microorganism under simulated indoor air conditions: Cu-Ag/TiO_2-based optical fibers at a pilot scale. Chem Eng J. 2021;411:128622. https://doi.org/10.1016/j.cej.2021.128622.
[13] Habibi-Yangjeh A, Asadzadeh-Khaneghah S, Feizpoor S, Rouhi A. Review on heterogeneous photocatalytic disinfection of waterborne, airborne, and foodborne viruses: can we win against pathogenic viruses? J Colloid Interface Sci. 2020;580:503. https://doi.org/10.1016/j.jcis.2020.07.047.
[14] Yang HL, Zou L, Juaim AN, Ma CX, Zhu MZ, Xu F, Chen XN, Wang YZ, Zhou XW. Copper release and ROS in antibacterial activity of Ti–Cu alloys against implant-associated infection. Rare Met. 2023;42(6):2007. https://doi.org/10.1007/s12598-022-02242-4.
[15] Zhang RQ, Song XH, Liu YY, Wang P, Wang ZY, Zheng ZK, Dai Y, Huang BB. Monomolecular VB_2-doped MOFs for photocatalytic oxidation with enhanced stability, recyclability and selectivity. J Mater Chem A. 2019;7:26934. https://doi.org/10.1039/C9TA09571C.
[16] Zeng XK, Liu Y, Xia Y, Uddin MH, Xia DH, McCarthy DT, Deletic A, Zhang XW. Cooperatively modulating reactive oxygen species generation and bacteria-photocatalyst contact over graphitic carbon nitride by polyethylenimine for rapid water disinfection. Appl Catal B-Environ. 2020;274:119095. https://doi.org/10.1016/j.apcatb.2020.119095.
[17] Li Q, Zhou QH, Shi L, Chen Q, Wang JL. Recent advances in oxidation and degradation mechanisms of ultrathin 2D materials under ambient conditions and their passivation strategies. J Mater Chem A. 2019;7:4291. https://doi.org/10.1039/C8TA10306B.
[18] Cai PF, Li J, Wu XB, Li ZY, Shen J, Nie JJ, Cui ZD, Chen DF, Liang YQ, Zhu SL, Wu SL. ALD-induced TiO_2/Ag nanofilm for rapid surface photodynamic ion sterilization. Rare Met. 2022;41(12):4138. https://doi.org/10.1007/s12598-022-02096-w.
[19] Dette C, Pérez-Osorio MA, Kley CS, Punke P, Patrick CE, Jacobson P, Giustino F, Jung SJ, Kern K. TiO_2 anatase with a bandgap in the visible region. Nano Lett. 2014;14:6533. https://doi.org/10.1021/nl503131s.
[20] Kang D, Kim TW, Kubota SR, Cardiel AC, Cha HG, Choi K-S. Electrochemical synthesis of photoelectrodes and catalysts for use in solar water splitting. Chem Rev. 2015;115(23):12839. https://doi.org/10.1021/acs.chemrev.5b00498.
[21] Ma Y, Le Formal F, Kafizas A, Pendlebury SR, Durrant JR. Efficient suppression of back electron/hole recombination in cobalt phosphate surface-modified undoped bismuth vanadate photoanodes. J Mater Chem A. 2015;3:20649. https://doi.org/10.1039/C5TA05826K.
[22] Zhao YB, Niu ZJ, Zhao JW, Xue L, Fu XZ, Long JL. Recent advancements in photoelectrochemical water splitting for hydrogen production. Electrochem Energy Rev. 2023;6:1. https://doi.org/10.1007/s41918-022-00153-7.
[23] Wu Z, Gong C, Yu J, Sun L, Xiao W, Lin C. Enhanced visible light photoelectrocatalytic activity over $Cu_xZn_{1-x}In_2S_4$@TiO_2 nanotube array hetero-structures. J Mater Chem A. 2017;5:1292. https://doi.org/10.1039/C6TA07420K.
[24] Wang XN, Zhang XC, Zhang Y, Wang Y, Sun S-P, Wu WD, Wu ZX. Nanostructured semiconductor supported iron catalysts for heterogeneous photo-Fenton oxidation: a review. J Mater Chem A. 2020;8:15513. https://doi.org/10.1039/D0TA04541A.
[25] Yang HL, Juaim AN, Zou L, Zhu MZ, Chen XN, Ma CX, Zhou XW. Antibacterial activity and mechanism of newly developed Zr–30Ta and Zr–25Ta–5Ti alloys against implant-associated infection. Rare Met. 2022;41(12):4176. https://doi.org/10.1007/s12598-022-02144-5.
[26] Nie X, Li GY, Gao MH, Sun HW, Liu XL, Zhao HJ, Wong P-K, An TC. Comparative study on the photoelectrocatalytic inactivation of Escherichia coli K-12 and its mutant *Escherichia coli* BW25113 using TiO_2 nanotubes as a photoanode. Appl Catal B-Environ. 2014;147:562. https://doi.org/10.1016/j.apcatb.2013.09.037.
[27] Zhang LL, Ma HK, Huang XM, Yan ZX, Ding W, Li ZF, Cang DQ. Fast and efficient inactivation of antibiotic resistant *Escherichia coli* by iron electrode-activated sodium peroxydisulfate in a galvanic cell. Chem Eng J. 2019;355:150. https://doi.org/10.1016/j.cej.2018.08.065.
[28] Wang MK, Zhu J, Zi Y, Wu ZG, Hu HG, Xie ZJ, Zhang Y, Hu LP, Huang WC. Functional two-dimensional black phosphorus nanostructures towards next-generation devices. J Mater Chem A. 2021;9:12433. https://doi.org/10.1039/D1TA02027G.
[29] Lu PS, Wu DX, Chen LQ, Li H, Wu F. Air stability of solid--state sulfide batteries and electrolytes. Electrochem Energy Rev. 2022;5:1. https://doi.org/10.1007/s41918-022-00149-3.
[30] Zhang MM, Wang K, Zeng SH, Xu Y, Nie WY, Chen PP, Zhou YF. Visible light-induced antibacterial effect of MoS_2: effect of the synthesis methods. Chem Eng J. 2021;411:128517. https://doi.org/10.1016/j.cej.2021.128517.
[31] Jia JR, Zhai MK, Lv JJ, Zhao BX, Du HB, Zhu JJ. Nickel molybdenum nitride nanorods grown on Ni foam as efficient and stable bifunctional electrocatalysts for overall water splitting. ACS Appl Mater Interfaces. 2018;10:30400. https://doi.org/10.1021/acsami.8b09854.
[32] Ikram M, Umar E, Raza A, Haider A, Naz S, Ul-Hamid A, Haider J, Shahzadi I, Hassan J, Ali S. Dye degradation performance, bactericidal behavior and molecular docking analysis of Cu-doped TiO_2 nanoparticles. RSC Adv. 2020;10:24215. https://doi.org/10.1039/D0RA04851H.
[33] Liu JH, Zhang L, Li NX, Tian QW, Zhou JC, Sun YM. Synthesis of MoS_2 /$SrTiO_3$ composite materials for enhanced photocatalytic activity under UV irradiation. J Mater Chem A. 2015;3:706. https://doi.org/10.1039/C4TA04984E.
[34] Wang F, Ren F, Ma D, Mu P, Wei HJ, Xiao CH, Zhu ZQ, Sun HX, Liang WD, Chen JX, Chen LH, Li A. Particle and nanofiber shaped conjugated microporous polymers bearing hydantoin-substitution with high antibacterial activity for water cleanness. J Mater Chem A. 2018;6:266. https://doi.org/10.1039/C7TA09405A.
[35] Zhu T, Wu HB, Wang YB, Xu R, Lou XW. Formation of 1D hierarchical structures composed of Ni_3S_2 nanosheets on CNTs backbone for supercapacitors and photocatalytic H_2 production. Adv Energy Mater. 2012;2:1497. https://doi.org/10.1002/aenm.201200269.
[36] Chen Q, Xie F, Zhou H. Self-construction of core−shell and hollow zeolite analcime icositetrahedra: a reversed crystal growth process via oriented aggregation of nanocrystallites and recrystallization from surface to core. J Am Chem Soc. 2007;129:13305. https://doi.org/10.1021/ja074834u.
[37] Wang J, Chao DL, Liu JL, Li LL, Lai LF, Lin JY, Shen ZX. Ni_3S_2@MoS_2 core/shell nanorod arrays on Ni foam for high-performance electrochemical energy storage. Nano Energy. 2014;7:151. https://doi.org/10.1016/j.nanoen.2014.04.019.
[38] Yin C, Yang FL, Wang SL, Feng LG. Heterostructured $NiSe_2$/$MoSe_2$ electronic modulation for efficient electrocatalysis in urea assisted water splitting reaction. Chin J of Catal. 2023;51:225. https://doi.org/10.1016/S1872-2067(23)64490-0.
[39] Li M, Feng LG. $NiSe_2$-$CoSe_2$ with a hybrid nanorods and nanoparticles structure for efficient oxygen evolution reaction. Chin J Struct Chem. 2022;41:2201019. https://doi.org/10.14102/j.cnki.0254-5861.2021-0037.

[40] Wang SL, Zhao LY, Li JX, Tian XL, Wu X, Feng LG. High valence state of Ni and Mo synergism in NiS_2-MoS_2 hetero--nanorods catalyst with layered surface structure for urea electrocatalysis. J Energy Chem. 2022;66:483. https://doi.org/10.1016/j.jechem.2021.08.042.
[41] Schindra KR, Dhakal D, Hur J, Lee SW. Visible light driven MoS_2/α-$NiMoO_4$ ultra-thin nanoneedle composite for efficient Staphylococcus aureus inactivation. J Hazard Mater. 2020;385:121553. https://doi.org/10.1016/j.jhazmat.2019.121553.
[42] Mao JX, Liu P, Du CC, Liang DX, Yan JY, Song WB. Tailoring 2D MoS_2 heterointerfaces for promising oxygen reduction reaction electrocatalysis. J Mater Chem A. 2019;7:8785. https://doi.org/10.1039/C9TA01321K.
[43] Sivanantham A, Ganesan P, Shanmugam S. Hierarchical $NiCo_2S_4$ nanowire arrays supported on Ni foam: an efficient and durable bifunctional electrocatalyst for oxygen and hydrogen evolution reactions. Adv Funct Mater. 2016;26:4661. https://doi.org/10.1002/adfm.201600566.
[44] Zhang N, Lei JX, Xie JP, Huang HY, Yu Y. MoS_2/Ni_3S_2 nanorod arrays well-aligned on Ni foam: a 3D hierarchical efficient bifunctional catalytic electrode for overall water splitting. RSC Adv. 2017;7:46286. https://doi.org/10.1039/C7RA07667C.
[45] Li XQ, Feng S, Yang J, Xie TP, Wang JK, Chen XJ, Kong DS, Chen HY. Tetracycline removal by a magnetic heterojunction Cu_2O/$CoFe_2O_4$ activating peroxymonosulfate. Rare Met. 2023;42(3):862. https://doi.org/10.1007/s12598-022-02170-3.
[46] Kohansk MA, Dwyer DJ, Hayete B. Common mechanism of cellular death induced by bactericidal antibiotics. Cell. 2007;130:797. https://doi.org/10.1016/j.cell.2007.06.049.
[47] Dwyer DJ, Kohanski MA, Hayete B, Collins JJ. Gyrase inhibitors induce an oxidative damage cellular death pathway in Escherichia coli. Mol Syst Biol. 2007;3:91. https://doi.org/10.1038/msb4100135.
[48] Bédis D, Andréanne L, Michel GB, Philippe L, Marc O. Differences in antibiotic-induced oxidative stress responses between laboratory and clinical isolates of streptococcus pneumoniae. Agents Chemother. 2015;59:5420. https://doi.org/10.1128/aac.00316-15.
[49] Inoue M, Sato EF, Nishikawa M, Park AM, Kira Y, Imada I, Utsuml K. Mitochondrial generation of reactive oxygen species and its role in aerobic life. Curr Med Chem. 2003;10:2495. https://doi.org/10.2174/0929867033456477.
[50] Li YM, Meng LH, Hu YR, Zhang TT, Su ZN, Ouyang ZY, Li WC, Wan JL, Wu QZ. Suppression mechanisms on proliferation of glioma U251 cells by FePt nanoparticles through intracellular oxidative stress. Rare Met. 2022;41(4):1202. https://doi.org/10.1007/s12598-021-01885-z.
[51] Kwon HY, Choi SY, Won MH, Kang TC, Kang JH. Oxidative modification and inactivation of Cu, Zn-superoxide dismutase by 2,2′-azobis(2-amidinopropane) dihydrochloride. BBA Protein Struct Mol Enzymol. 2000;1543:69. https://doi.org/10.1016/S0167-4838(00)00197-7.
[52] Ray SK, Dhakal D, Regmi C, Yamaguchui T, Lee SW. Inactivation of *Staphylococcus aureus* in visible light by morphology tuned α-$NiMoO_4$. J Photochem Photobiol A: Chem. 2018;350:59. https://doi.org/10.1016/j.jphotochem.2017.09.042.
[53] Leung TY, Chan CY, Hu C, Yu JC, Wong PK. Photocatalytic disinfection of marine bacteria using fluorescent light. Water Res. 2008;42:4827. https://doi.org/10.1016/j.watres.2008.08.031.
[54] Chong Y, Ge CC, Fang G, Wu RF, Zhang H, Chai ZF, Chen CY, Yin JJ. Light-enhanced antibacterial activity of graphene oxide, mainly via accelerated electron transfer. Environ Sci Technol. 2017;51:10154. https://doi.org/10.1021/acs.est.7b00663.
[55] Li CJ, Shan GC, Guo CX, Ma RG. Design strategies of Pd-based electrocatalysts for efficient oxygen reduction. Rare Met. 2023;42(6):1778. https://doi.org/10.1007/s12598-022-02234-4.
[56] Baaloudj O, Assadi AA, Azizi M, Kenfoud H, Trari M, Amrane A, Assadi AA, Nasrallah N. Synthesis and characterization of $ZnBi_2O_4$ nanoparticles: photocatalytic performance for antibiotic removal under different light sources. Appl Sci. 2021;11:3975. https://doi.org/10.3390/app11093975.